Improved Thermoelectric Performance in $Yb_{14}Mn_{1-x}Zn_xSb_{11}$ by the Reduction of Spin-Disorder Scattering

Shawna R. Brown,[†] Eric S. Toberer,[‡] Teruyuki Ikeda,[‡] Catherine A. Cox,[†] Franck Gascoin,[‡,§,⊥] Susan M. Kauzlarich,*[,†] and G. Jeffrey Snyder*[,‡,§]

Department of Chemistry, University of California, One Shields Avenue, Davis, California 95616, Jet Propulsion Laboratory, California Institute of Technology, 4800 Oak Grove Drive, Pasadena, California 91109-8099, and Materials Science, California Institute of Technology, 1200 California Boulevard, Pasadena, California 91125

Received December 19, 2007. Revised Manuscript Received February 9, 2008

Rare-earth transition metal compounds $Yb_{14}Mn_{1-x}Zn_xSb_{11}$, isostructural with $Ca_{14}AlSb_{11}$, have been prepared using a metal flux growth technique for thermoelectric property measurements (with $x = 0.0$, 0.2, 0.3, 0.4, 0.7, 0.9, and 1.0). Single-crystal X-ray diffraction and electron microprobe analysis data indicate the successful synthesis of a solid-solution for the $Yb_{14}Mn_{1-x}Zn_xSb_{11}$ structure type for $0 < x < 0.4$. Hot-pressed polycrystalline samples showed that the product from the flux reaction was a pure phase from $x = 0$ through $x = 0.4$ with the presence of a minor secondary phase for compositions $x > 0.4$. High-temperature (298 K–1275 K) measurements of the Seebeck coefficient, resistivity, and thermal conductivity were performed on hot-pressed, polycrystalline samples. As the concentration of Zn increases in $Yb_{14}Mn_{1-x}Zn_xSb_{11}$, the Seebeck coefficient remains unchanged for $0 \leq x \leq 0.7$ indicating that the free carrier concentration has remained unchanged. However, as the nonmagnetic Zn^{2+} ions replace the magnetic Mn^{2+} ions, the spin disorder scattering is reduced, lowering the resistivity. Replacing the magnetic Mn^{2+} with non magnetic Zn^{2+} provides an independent means to lower resistivity without deleterious effects to the Seebeck values or thermal conduction. Alloying the Mn site with Zn reduces the lattice thermal conductivity at low temperatures but has negligible impact at high temperatures. The reduction of spin disorder scattering leads to an ~10% improvement over $Yb_{14}MnSb_{11}$, revealing a maximum thermoelectric figure of merit (zT) of ~1.1 at 1275 K for $Yb_{14}Mn_{0.6}Zn_{0.4}Sb_{11}$.

Introduction

Humanity's demand for energy resources causes much of the social, political, and environmental difficulties we are experiencing. A new energy landscape is needed based on sustainable, environmentally benign energy sources. Thermoelectric generators, which utilize the flow of heat through a material to generate power, have seen renewed interest because of their potential to provide a sustainable energy solution via harvesting of waste heat and cogeneration. The reliability of thermoelectric generators has been proven through NASA missions such as Voyager, where thermoelectric generators have operated unattended for more than 30 years. Vital for the widespread terrestrial use of thermoelectrics is an improvement in their conversion efficiencies. The root of these low efficiencies is poor material efficiencies and as such, much of the research on thermoelectrics is devoted to the search for new materials and the optimization of known good thermoelectric materials. This search has led to the discovery of several complex structure types with exceptional thermoelectric properties.[1–4]

High-temperature thermoelectric power generation applications are limited by the lack of a good *p*-type leg material. While NASA has used a *p*-type $Si_{1-x}Ge_x$ alloy (SiGe) with $x \approx 0.3$, the maximum figure of merit (zT) of 0.6 results in poor conversion efficiency.[5] The discovery of $Yb_{14}MnSb_{11}$ with a maximum zT of ~1.0 at 1223 K represents a significant improvement over *p*-type SiGe.[3] Considering the chemical variety of materials isostructural with $Yb_{14}MnSb_{11}$, the zT may be further improved through alloying the parent compound.

In a thermoelectric device, two parameters primarily govern the efficiency-the thermoelectric figure of merit (zT) and the temperature difference (ΔT). The material's figure of merit (zT, Equation 1) depends on the Seebeck coefficient (α), electrical resistivity (ρ), thermal conductivity (κ). The Carnot efficiency sets the maximum efficiency limit, $\eta_c = \Delta T / T_{hot}$. The actual device efficiency is thus the product of the

* To whom correspondence should be addressed. E-mail: smkauzlarich@ucdavis.edu (S.M.K.); jsnyder@caltech.edu (G.J.S.).
† University of California.
‡ Jet Propulsion Laboratory, California Institute of Technology.
§ Materials Science, California Institute of Technology.
⊥ Current contact information: Laboratoire de Physico-Chimie de la Matière Condensée, Université Montpellier 2, place Eugène Bataillon, 34095 Montpellier Cedex 5, France.

(1) Sales, B. C.; Mandrus, D.; Williams, R. K. *Science (Washington, D.C.)* **1996**, *272*, 1325.
(2) Nolas, G. S.; Cohn, J. L.; Slack, G. A.; Schujman, S. B. *Appl. Phys. Lett.* **1998**, *73*, 178.
(3) Brown, S. R.; Kauzlarich, S. M.; Gascoin, F.; Snyder, G. J *Chem. Mater.* **2006**, *18*, 1873.
(4) Caillat, T.; Fleurial, J. P.; Borshchevsky, A. *J. Phys. Chem. Solids* **1997**, *58*, 1119.
(5) Vining, C. B. In *CRC Handbook of Thermoelectrics*; Rowe, M., Ed.; CRC Press: Boca Raton, FL, 1995; p 329.

10.1021/cm703616q CCC: $40.75
Published on Web 04/24/2008

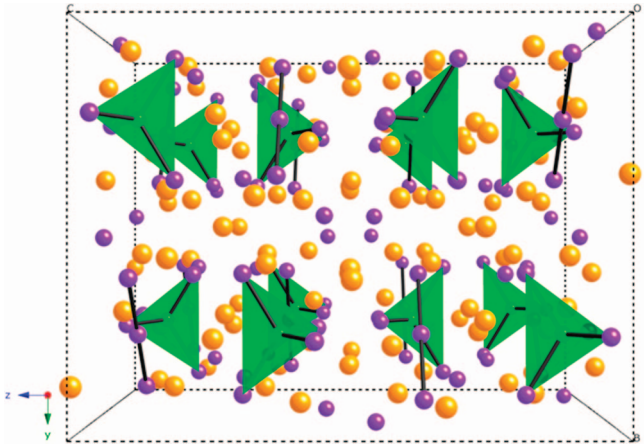

Figure 1. A view of the crystal structure of $Yb_{14}Mn_{1-x}Zn_xSb_{11}$ down the *a* axis, showing the $[Mn_{1-x}Zn_xSb_4]^{9-}$ tetrahedra, the $[Sb_3]^{7-}$ polyatomic anions, Sb^{3-} anions, and Yb^{2+} cations. The green polyhedra represent ($Mn_{1-x}Zn_x$) and the orange and purple spheres represent Yb and Sb, respectively.

Carnot efficiency and the reduced efficiency which is a function of zT.[6,7]

$$zT = \frac{\alpha^2 T}{\rho\kappa} \quad (1)$$

In addition to zT, in order to obtain high efficiency over a large temperature gradient, the thermoelectric compatibility factor (s, Equation 2) needs to be considered. Similar compatibility factors (s) between adjacent materials in a segmented device promote a high overall efficiency for the device. If the compatibility factor of two materials differ by more than a factor of 2, segmentation of the materials will lead to an efficiency for the device significantly lower than that expected from its zT value.[8]

$$s = \frac{\sqrt{1+zT}-1}{\alpha T} \quad (2)$$

The $A_{14}MPn_{11}$ family of compounds possess a complex unit cell (Figure 1) where the stoichiometry and electron counting can be understood using the Zintl formalism as consisting of one $[MPn_4]^{9-}$ tetrahedron, one $[Pn_3]^{7-}$ polyatomic anion, four Pn^{3-} anions, and 14 A^{2+} cations per formula unit (A = Ca, Sr, Ba, Yb, Eu; M = Mn, Zn, Al, Ga, In; Pn = P, As, Sb, Bi).[3,7,9–18] In a Zintl compound, these covalently bonded units are held together via ionic forces. The $A_{14}MPn_{11}$ phases can also be considered as polar intermetallics where the Zintl formalism holds, but charge transfer is not complete. Here, the ionic picture serves the purpose for electron counting. When the A element is 2+ and the M element is 3+, as in the originating compound of this family, $Ca_{14}AlSb_{11}$, a semiconducting Zintl phase results.[19]

The magnetic and electronic properties of $Yb_{14}MnSb_{11}$ are consistent with high spin d^5 Mn^{2+} and one spin-paired hole per formula unit. To satisfy the Zintl formalism, one might expect d^4 Mn^{3+}, because the magnetization measurements of $Yb_{14}MnSb_{11}$ are consistent with an $s = 2$ local moment, but such a description does not explain the p-type conductivity with one hole per formula unit.[13,20,21] Likewise, theoretical calculations,[22] XPS,[13] X-ray magnetic circular dichroism (XMCD),[14] doping studies,[15] and optical studies[17] have concluded the Mn is 2+ with an associated hole in the Sb p orbital. The magnetization measurements may be understood as a screening or antialignment of a Sb 5p hole with the five 3d electrons in Mn^{2+}, reducing the net spin to $s = 2$.[22] The increasing resistivity and Seebeck coefficient with increasing temperature indicate the hole is delocalized.[3] This antiferromagnetic interaction has been described as a Kondo interaction[15] with $T_K \sim 285$ K and $Yb_{14}MnSb_{11}$ as a rare example of an underscreened Kondo lattice.

$Yb_{14}ZnSb_{11}$ is somewhat less resistive than $Yb_{14}MnSb_{11}$ despite the isoelectronic nature of the Zn^{2+} substitution for Mn^{2+}.[23] A significant portion of the electrical resistance in $Yb_{14}MnSb_{11}$ has previously been shown to be due to spin disorder scattering from the unpaired Mn^{2+} d^5 electrons.[21,23] Spin disorder scattering in $Yb_{14}ZnSb_{11}$ does not result from d^{10} Zn^{2+} because it has zero spin; instead, $Yb_{14}ZnSb_{11}$ exhibits spin disorder scattering in the electrical resistivity due to Yb valence fluctuations.[21,23] Low temperature magnetic and electronic data provide evidence that $Yb_{14}ZnSb_{11}$ has a Zn oxidation state of 2+ with a delocalized hole partially in the Yb f orbital. XPS confirms that the ytterbium is of mixed valence, Yb^{2+} and Yb^{3+}.[13,23] No such Yb valence fluctuations are observed in $Yb_{14}MnSb_{11}$; the delocalized hole resides in the Sb and Mn bands.[22]

As the spin disorder scattering adds to the electrical resistivity, a clear route to improved zT of $Yb_{14}MnSb_{11}$ would employ replacing Mn^{2+} with a nonmagnetic isoelectronic ion that maintains the carrier concentration and the electronic structure. It is well-known that d^{10} Zn^{2+} can be substituted for magnetic ions in ferrimagnetic oxides to alter the magnetic properties.[24] In this paper, we show that the

(6) Rowe, D. M., Ed.; CRC Press: Boca Raton, FL, 2006.
(7) Kauzlarich, S. M.; Payne, A. C.; Webb, D. J. In *Magnetism: Molecules to Materials III*; Miller, J. S., Drillon, M., Eds.; Wiley-VCH: Weinham, Germany, 2002; p 37.
(8) Snyder, G. J.; Ursell, T. S. *Phys. Rev. Lett.* **2003**, *91*, 148301.
(9) Kauzlarich, S. M. *Comm. Inorg. Chem.* **1990**, *10*, 75.
(10) Kauzlarich, S. M. In *Chemistry, Structure, and Bonding of Zintl Phases and Ions*; Kauzlarich, S., Ed.; VCH Publishers: New York, 1996; p 245.
(11) Kim, H.; Kauzlarich, S. M. *J. Solid State Chem.* **2005**, *178*, 1935.
(12) Fisher, I. R.; Wiener, T. A.; Bud'ko, S. L.; Canfield, P. C.; Chan, J. Y.; Kauzlarich, S. M. *Phys. Rev. B: Condens. Matter Mater. Physics* **1999**, *59*, 13829.
(13) Holm, A. P.; Ozawa, T. C.; Kauzlarich, S. M.; Morton, S. A.; Waddill, G. D.; Tobin, J. G. *J. Solid State Chem.* **2005**, *178*, 262.
(14) Holm, A. P.; Kauzlarich, S. M.; Morton, S. A.; Waddill, G. D.; Pickett, W. E.; Tobin, J. G. *J. Am. Chem. Soc.* **2002**, *124*, 9894.
(15) Sales, B. C.; Khalifah, P.; Enck, T. P.; Nagler, E. J.; Sykora, R. E.; Jin, R.; Mandrus, D. *Phys. Rev. B* **2005**, 72.
(16) Srinath, S.; Poddar, P.; Srikanth, H.; Sales, B. C.; Mandrus, D. *Phys. Rev. Lett.* **2005**, 95.
(17) Burch, K. S.; Schafgans, A.; Butch, N. P.; Sayles, T. A.; Maple, M. B.; Sales, B. C.; Mandrus, D.; Basov, D. N. *Phys. Rev. Lett.* **2005**, 95.
(18) Sales, B. C.; Jin, R. Y.; Mandrus, D.; Khalifah, P. *Phys. Rev. B* **2006**, 73.
(19) Cordier, G.; Schäfer, H.; Stelter, M. *Z. Anorg. Allg. Chem.* **1984**, *519*, 183.
(20) Chan, J. Y.; Olmstead, M. M.; Kauzlarich, S. M.; Webb, D. J. *Chem. Mater.* **1998**, *10*, 3583.
(21) Ribeiro, R. A.; Hadano, Y.; Narazu, S.; Suekuni, K.; Avila, M. A.; Takabatake, T. *J. Phys: Condens. Matter* **2007**, *19*, 376211.
(22) Sánchez-Portal, D.; Martin, R. M.; Kauzlarich, S. M.; Pickett, W. E. *Phys. Rev. B* **2002**, *65*, 144414.
(23) Fisher, I. R.; Bud'ko, S. L.; Song, C.; Canfield, P. C.; Ozawa, T. C.; Kauzlarich, S. M. *Phys. Rev. Lett.* **2000**, *85*, 1120.
(24) Cullity, B. D. *Introduction to Magnetic Materials*; Addison-Wesley, Reading, PA, 1972.

substitution of Zn for Mn in $Yb_{14}MnSb_{11}$ reduces the spin-disorder scattering without inducing Yb valance fluctuations. This significantly reduces the resistivity but the Seebeck coefficient remains unaffected. Such a decoupling of the resistivity and Seebeck coefficient is rarely seen in thermoelectric materials.

Experimental Section

Single-Crystal Synthesis. All materials were handled in a nitrogen-filled drybox with water levels below 1.0 ppm. Sublimed dendritic Yb metal (Alfa Aesar, 99.99%) was cut into small pieces. Mn chips (Alfa Aesar, 99.98%) were ground into a powder. Zn powder (Fisher, 99.4%), Sb chunks (Allied Chemical, 99.7%) and Sn granules (Mallinckrodt, 99.967%) were used as received. All of the $Yb_{14}Mn_{1-x}Zn_xSb_{11}$ solid solutions were prepared by way of a Sn-flux method that has been previously published.[12,23] The elements, Yb:Mn:Zn:Sb:Sn, were arranged in 10 cm^3 Al_2O_3 crucibles in the molar ratios 14:6−*a*:*a*:11:86 (where *a* is an integer from 0 to 6). Throughout this manuscript, x_{syn} is used to designate the molar ratio $m_{Zn}/(m_{Mn} + m_{Zn})$ used in the flux reaction for any discussion of samples prior to the completion of the structural analyses (i.e., X-ray diffraction and microprobe analysis). The mixtures were sealed in quartz ampoules under vacuum atmosphere and placed in high-temperature programmable furnaces. The reactions were brought up to 1375 K following the heating procedure presented by Fisher et al. in 1999.[12] Once at 1375 K the reactions were held for 1 h, and then cooled to temperatures between 975 and 1075 K. Upon reaching final temperatures, the mixtures were inverted and spun in a centrifuge to separate the Sn-flux from the single-crystal products. High yields of reflective, silver colored single-crystal ingots were obtained.

Single-Crystal X-ray Diffraction. While in a nitrogen-filled dry box, single crystals of $Yb_{14}Mn_{1-x}Zn_xSb_{11}$ were selected and placed under mineral oil for transport to the diffractometer in order to prevent oxidation of the sample. A suitable crystal was selected, positioned at the end of a glass fiber, and quickly placed in a nitrogen (low temperature) stream. Diffraction data for $Yb_{14}Mn_{1-x}Zn_xSb_{11}$ were collected at 90 K on a Bruker SMART 1000 system. Mo Kα (0.71073 Å) radiation and CCD area detector were used. Data acquisition was performed with SMART software and data reduction performed with SAINT version 6.45. Multiscan absorption correction was applied to the series of compounds using SADABS. The initial atom positions were obtained using direct methods, and refined with SHELXTL version 5.1. The data were refined four different ways and the resulting R's, U's, and peak/hole values reviewed. (1) Occupancies of the shared Mn/Zn site were allowed to vary; (2) Zn occupancy (*x*) was fixed to that obtained from the single crystal microprobe results and Mn occupancy was fixed at 1−*x*; (3) Zn and Mn occupancies were fixed to the expected values based on the stoichiometry used in the reaction; and (4) Zn and Mn occupancies were fixed to the average microprobe results, *x*. In all refinements, the R's, U's, and peak/hole differences were fairly similar, suggesting that the refinement was insensitive to the specific values of Mn and Zn. This is probably a consequence of the small amount of Mn/Zn in the structure relative to the large number of heavy atoms. The refinement using Zn from the single crystal microprobe results was deemed the most reasonable model and that is presented herein. The data collection parameters and CIFs are provided in the Supporting Information.

Electron Microprobe Analysis. Microprobe analysis was conducted using a Cameca SX-100 Electron Probe Microanalyzer equipped with a wavelength-dispersive spectrometer. The samples were prepared by mounting approximately five $Yb_{14}Mn_{1-x}Zn_xSb_{11}$ crystals onto 25 mm metal rounds by means of adhesive carbon tape. Net elemental intensities for Yb, Mn, Zn, and Sb were determined with respect to pure elemental calibration standards that were polished before analysis to ensure that the elements were not oxidized. Because the crystals were grown in a Sn-flux, Sn concentration was also checked to ensure that no incorporation of Sn took place in the crystal growing process. There was no evidence of Sn present. Each crystal was scanned at ∼10 points along its surface with a spot size of 1 μm. Elemental totals for all analyses were 100 ± 2% mass percent. Each composition resulted in individual elemental percentages that were either identical or within standard deviation of one another, when compared with crystals of the same stoichiometry from different reactions.

Electron microprobe analysis was also performed on the hot-pressed samples using a JEOL JXA-8200 electron probe microanalyzer equipped with a wavelength-dispersive spectrometer under the accelerating voltage of 15 kV. Before analysis, samples were mounted in epoxy pucks and surfaces were polished with 0.3 μm alumina paste in isopropyl alcohol. Pure metals or compounds of Mn, Zn, Sb, and $YbPO_4$ were used as standard samples for the ZAF conversion from the X-ray intensities of Mn K_α, Zn K_α, Sb L_α, and Yb L_α to chemical compositions.

Differential Thermal Analysis and Thermogravimetry Measurements (DTA/TG). A Netzsch Thermal Analysis STA 409 cell, equipped with a TASC 414/2 controller and PU 1.851.01 power unit was used to evaluate the thermal properties of $Yb_{14}MnSb_{11}$ and $Yb_{14}ZnSb_{11}$ between 298 and 1373 K. After a baseline was established, single crystals (30–50 mg) were placed in BN crucibles and heated at 10 K/min under flowing argon with an acquisition rate of 2.0 pts/K. Data were acquired using the software provided with the instrument. Analysis was performed using the computer program, Netzsch Proteus Analysis.

Thermoelectric Properties Sample Preparation. To obtain dense samples, we hot-pressed the finely ground polycrystalline powder in high-density graphite dies (POCO). Cylinders about 6.5 mm long and 12 mm in diameter were thus obtained. The densities (calculated from measured dimensions and weight) were found to be about 95% of the theoretical density. The hot-pressing for all samples was conducted at a pressure of about 1.38×10^8 Pa and at 1223 K for 1.5 h under an argon atmosphere.

Samples in the form of discs (typically 1 mm thick and 12 mm diameter slice) were cut from the cylinder using a diamond saw for electrical and thermal transport properties, whereas the Seebeck coefficient was measured on the remaining cylinder. Most of these physical properties were measured between room temperature and 1273 K.

Resistivity Measurements. The electrical resistivity (ρ) was measured using the van der Pauw technique with a current of 100 mA using a special high-temperature apparatus.[25] The Hall coefficient was measured in the same apparatus with a constant magnetic field value of about 10 100 Gauss. The carrier density was calculated from the Hall coefficient (R_H) assuming a scattering factor of 1.0 in a single carrier scheme, by $n = 1/R_H e$, where *n* is the density of holes, and *e* is the charge of the electron. The Hall mobility (μ_H) was calculated from the Hall coefficient and the resistivity values with $\mu_H = R_H/\rho$.

Thermal Conductivity Measurements. The thermal diffusivity was measured using a flash diffusivity technique.[26] Heat capacity (C_p) was estimated using the method of Dulong-Petit with a value of 0.169 J/(gK). The thermal conductivity (κ) was then calculated

(25) McCormack, J. A.; Fleurial, J. P. *Mater. Res. Soc. Symp. Proc.* **1991**, *234*, 135.
(26) Vandersande, J. W.; Wood, C.; Zoltan, A.; Whittenberger, D. *Therm. Cond.* **1988**, *19*, 445.

from the experimental density, heat capacity, and the thermal diffusivity.

Seebeck Measurements. For all samples except $Yb_{14}ZnSb_{11}$, the Seebeck coefficient (α) was measured up to 1273 K using a high-temperature light pulse technique.[27] For $Yb_{14}ZnSb_{11}$ the Seebeck coefficient was measured to 1100 K. W/Nb thermocouples were used to measure the temperature and the Nb thermocouple legs were used to measure the voltage across the sample. The absolute Nb voltage was subtracted from the measured voltage. A pulsing temperature difference of 5 K was generated and the slope of the voltage versus ΔT used to calculate the Seebeck coefficient.

Figure of Merit Calculations. The temperature dependence of the resistivity data was fit using a linear equation ($\rho = \rho_o + \rho_1 T$). As samples with the experimentally determined composition $0.0 \leq x \leq 0.7$ had nearly identical Seebeck coefficients ($\pm 5\%$), a single polynomial curve (6th order) was fit to the union of this data. For experimentally determined compositions $x = 0.9$ and 1.0, the trends in Seebeck coefficient with temperature were fit using polynomial curves. To eliminate scatter in the thermal conductivity values used for the zT calculation, for experimental $x < 1.0$ the electronic component (κ_e) was added to the lattice component of $Yb_{14}MnSb_{11}$. These calculated κ curves are provided in the Supporting Information.

Results and Discussion

Phase Characterization. Large samples (6–8 g) of $Yb_{14}Mn_{1-x}Zn_xSb_{11}$ were prepared using a metal flux growth technique. A 6-fold excess of transition metals (Mn, Zn) was used during the synthesis, recognizing that much is incorporated into the flux. As this incorporation into the flux can change the Mn−Zn ratio, determination of the exact final composition is vital. Two designations of "*x*" are used in the following discussion to designate the specific sample of the doped system; x_{syn}, the molar ratio $m_{Zn}/(m_{Mn} + m_{Zn})$; and *x*, the ratio of Mn/Zn from microprobe analysis.

The product of each $Yb_{14}Mn_{1-x}Zn_xSb_{11}$ reaction was characterized by single crystal X-ray diffraction. All of the single-crystal structure data refined well with low R's and satisfactory residuals and showed that the compounds are isostructural to $Yb_{14}MnSb_{11}$, which has previously been described in detail.[20] The majority of the solid-solution samples ($x_{syn} = 0.17$, 0.33, 0.5, 0.83) follow the expected trend (Figure 2) of the previously published lattice parameters for the two end members, $Yb_{14}MnSb_{11}$ and $Yb_{14}ZnSb_{11}$.[20,23] In general, the lattice parameters decrease with increasing *x* as would be expected because of the slightly smaller radius of Zn^{2+} (0.60 Å) compared to that of Mn^{2+} (0.66 Å).[28] Figure 2 illustrates the x_{syn} of the solid-solutions versus their respective *a*(Å) and *c*(Å) axes, as well as for the volume. The *a* axis changed very little throughout the series, whereas the *c* axis consistently decreased. This plot clearly shows that the unit cells follow a downward sloping linear trend through $x_{syn} = 0.5$ that is consistent with Vegard's law, indicating that this system should be a solid solution.

The single-crystal X-ray diffraction structures refined well with the Mn/Zn occupancy fixed to the value obtained for Zn from the single crystal microprobe results described below. Structural deviations were consistent with Zn replacement of Mn, revealing slight decrease in the tetrahedral bond length, from 2.7422(6) for $x_{syn} = 0.17$ to 2.7334(6) Å for $x_{syn} = 0.83$. The angles for the tetrahedron remain unchanged throughout the series, consistent with the isoelectronic substitution of Mn^{2+} by Zn^{2+}. The distances within the Sb_3^{7-} unit also remained basically unchanged with bond length of 3.1878 (8) Å for $x = 0.2$ to 3.1823 (8) Å for $x = 0.9$. It has been proposed that the smaller unit cell for the Zn compound is due to the presence of Yb^{3+},[23] so the Sb−Yb bond lengths and angles were also reviewed. Throughout the series of bond lengths, changes were consistently less than 5% for all atoms, and no Yb−Sb bond lengths showed exceptional changes that might be attributed to a Yb valence change.

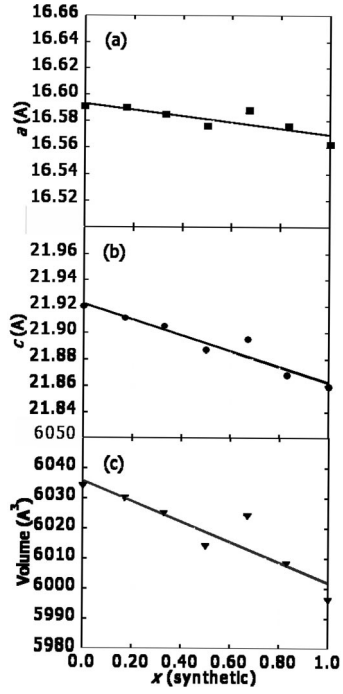

Figure 2. Single-crystal X-ray diffraction lattice parameters for $Yb_{14}Mn_{1-x}Zn_xSb_{11}$, (a) *a*(Å) (squares) is presented in the top plot, (b) *c* (Å) (circles) is presented in the middle plot, and (c) volume (Å^3) (triangles) is presented in the bottom plot. *x*-axis represents x_{syn}, the molar ratio $m_{Zn}/(m_{Mn} + m_{Zn})$ used in the synthesis.

Table 1 shows a comparison of the elemental analysis from single-crystal X-ray diffraction refinement and electron microprobe data for both single crystals and hot pressed pellets. The end member single-crystal data were not collected. Microprobe results for the single crystals and the hot pressed pellets are similar. Figure 3 presents electron microprobe backscattered images of the hot-pressed slices that are representative of the areas analyzed for each composition. The black sections of the images are gaps or holes within the hot-pressed slices. For the majority of the compounds presented, these images are consistent with homogeneous compounds. The single-crystal microprobe analysis was performed on approximately five crystals for each compound and represents an average of 40 points for each element, so that the standard deviations are quite low. The results are consistent with the analysis from the hot-pressed pellets. Each analysis provides average values for the crystals measured and are presented in Table 1. The single-crystal microprobe results show that when $x_{syn} = 0.5$, at least one crystal corresponding to the $Yb_9M_{4+x}Sb_9$

(27) Wood, C.; Zoltan, D.; Stapfer, G. *Rev. Sci. Instrum.* **1985**, *56*, 719.
(28) Shannon, R. D. *Acta Crystallogr., Sect. A* **1976**, *32*, 751.

Table 1. Comparisons of Elemental Analysis from Single-Crystal X-ray Diffraction, and Electron Microprobe Data from Single Crystals and Hot-Pressed Pellets

			microprobe on hot-pressed pellets	
x_{syn}[a]	single crystal diffraction[b]	microprobe on single crystals	majority phase	minority phase[c]
0.0	$Yb_{14}MnSb_{11}$		$Yb_{14}Mn_{1.01}Sb_{10.79}$	
0.17	$Yb_{14}Mn_{0.78}Zn_{0.22}Sb_{11}$	$Yb_{14.0(2)}Mn_{1.02(2)}Zn_{0.22(2)}Sb_{11.09(23)}$		
0.33	$Yb_{14}Mn_{0.77}Zn_{0.23}Sb_{11}$	$Yb_{14.0(5)}Mn_{0.91(3)}Zn_{0.23(2)}Sb_{10.57(41)}$	$Yb_{14}Mn_{0.89}Zn_{0.27}Sb_{10.95}$	
0.5	$Yb_{14}Mn_{0.67}Zn_{0.33}Sb_{11}$	$Yb_{14.0(3)}Mn_{0.77(3)}Zn_{0.33(5)}Sb_{10.66(29)}$ $Yb_{9.0(3)}Mn_{1.4(1)}Zn_{2.4(2)}Sb_{8.3(3)}$	$Yb_{14}Mn_{0.77}Zn_{0.36}Sb_{10.76}$	
0.67	$Yb_{14}Mn_{0.32}Zn_{0.68}Sb_{11}$		$Yb_{14.0}Mn_{0.45}Zn_{0.68}Sb_{11.36}$	$Yb_{9.0}Zn_{3.18}Mn_{0.90}Sb_{8.86}$
0.83	$Yb_{14}Mn_{0.19}Zn_{0.81}Sb_{11}$	$Yb_{14.0(3)}Mn_{0.37(3)}Zn_{0.81(8)}Sb_{10.9(3)}$	$Yb_{14.0}Mn_{0.32}Zn_{0.92}Sb_{10.92}$	$Yb_{9.0}Zn_{3.47}Mn_{0.98}Sb_{8.70}$

[a] Molar ratio $m_{Zn}/(m_{Mn} + m_{Zn})$ used in synthesis. [b] Zn occupancy was fixed to the value obtained from single crystal microprobe for all samples, except $x = 0.7$, where the value from hot-pressed pellets was used. [c] Corresponds to darker region from backscattered electrons.

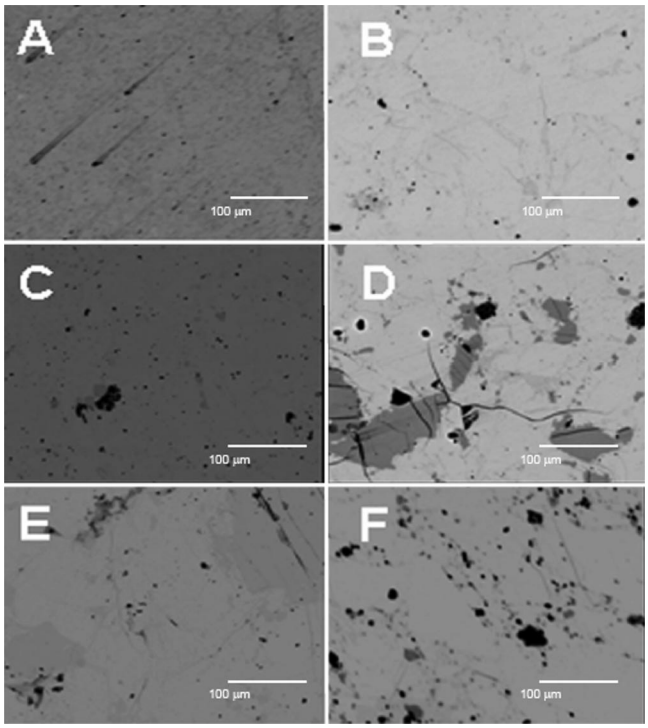

Figure 3. Representative electron microprobe images of hot pressed slices for x_{syn} (A) $x_{syn} = 0.0$, (B) $x_{syn} = 0.17$, (C) $x_{syn} = 0.33$, (D) $x_{syn} = 0.5$, (E) $x_{syn} = 0.83$, and (F) $x_{syn} = 1.0$.Bar indicates 100 μm.

phase[29,30] (M = Zn/Mn) was present (Table 1). For two of the hot-pressed samples, $x_{syn} = 0.67$ and $x_{syn} = 0.83$, the $Yb_9M_{4+x}Sb_9$ phase was detected through color variations in the backscattered images and the stoichiometry confirmed by microprobe analysis (Figure 3). This impurity phase must be fairly minor in the $x_{syn} = 0.5$ sample, as it was not identified in the hot pressed sample. This phase is present at ~20 and ~5% volume percent for the $x_{syn} = 0.67$ and $x_{syn} = 0.83$ samples, respectively (estimates determined visually).

Figure 4 provides the microprobe values of the experimentally determined x for the single crystal samples and the hot pressed pellets vs the idealized (synthetic) value, x_{syn}. The Mn/Zn ratio as determined by microprobe is frequently less than that used in the synthesis but does not change significantly with hot pressing. For example, in the highest Zn doped sample, $x = 0.9$ (experimental), the microprobe results from the single crystal samples and the hot pressed pellets provide similar values for the amount of Zn present

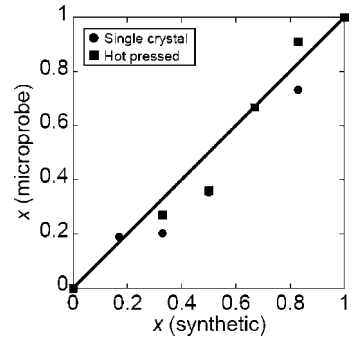

Figure 4. Experimental x for $Yb_{14}Mn_{1-x}Zn_xSb_{11}$ as determined from electron microprobe of the single crystals (circles) and hot pressed pellets (squares).

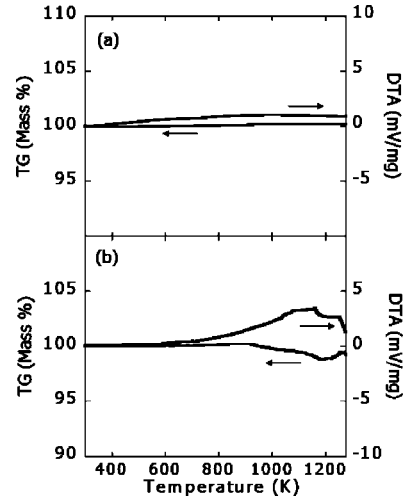

Figure 5. Differential thermal analysis (DTA) and thermogravimetry (TG) data collected at 10 K/min under flowing argon for (a) $Yb_{14}MnSb_{11}$ and (b) $Yb_{14}ZnSb_{11}$.

($Yb_{14}Mn_{0.37}Zn_{0.81}Sb_{11}$ versus $Yb_{14}Mn_{0.32}Zn_{0.92}Sb_{11}$). The differences may be attributed to the standards used and the particular instrumental parameters. For the remainder of this paper, the solid solution compounds will be referred to as the experimentally determined values, x. The hot pressed microprobe values of x are used for all compounds except for $x = 0.2$ which was determined by single crystal X-ray microprobe analysis only (0.0, 0.2, 0.3, 0.4, 0.7, 0.9, 1.0).

Figures 5a and 5b provide the DTA/TG measurements for $Yb_{14}MnSb_{11}$ and $Yb_{14}ZnSb_{11}$, respectively. It is evident that both materials do not reach a melting point before ~1175 K. The DTA/TG data for $Yb_{14}MnSb_{11}$ reveal neither phase changes nor sample instability. Both the DTA/TG data for $Yb_{14}ZnSb_{11}$ reveal that at elevated temperatures beyond 800

(29) Bobev, S.; Thompson, J. D.; Sarrao, J. L.; Olmstead, M. M.; Hope, H.; Kauzlarich, S. M. *Inorg. Chem.* **2004**, *43*, 5044.
(30) Xia, S. Q.; Bobev, S. *J. Am. Chem. Soc.* **2007**, *129*, 10011.

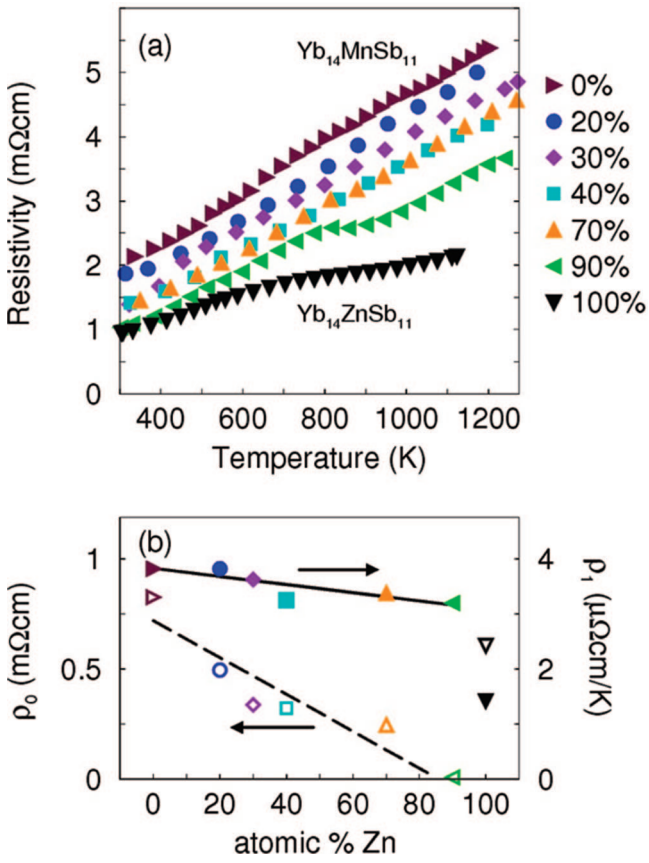

Figure 6. (a) Electrical resistivity measurements of the $Yb_{14}Mn_{1-x}Zn_xSb_{11}$ solid solution to 1273 K for all samples except for $Yb_{14}ZnSb_{11}$ which was measured to 1125 K. (b) Parameters resulting from a fit curve of the linear temperature dependence ($\rho_o + \rho_1 T$). Colors and symbols for the compositions are indicated in (b).

K the sample becomes unstable with a total mass loss of ~2% (max at 1200 K), likely due to the vaporization of the Zn from the compound.

Thermoelectric properties The thermoelectric properties of $Yb_{14}Mn_{1-x}Zn_xSb_{11}$ were obtained on the hot pressed pellets described above.

All samples display a linearly increasing resistivity with increasing temperature, as shown in Figure 6a (fit with $\rho = \rho_o + \rho_1 T$). This is expected from a metal or heavily doped semiconductor. Increasing the concentration of Zn lowers the temperature-independent term, ρ_o (open symbols, $T = 0$ K extrapolation), of the resistivity curve (Figure 6b) but has minimal impact on the slope, ρ_1 (closed symbols). For the $x = 0.9$ and 1.0 compounds it is observed that a subtle decrease in slope occurs at ~800 K, possibly due to a slight loss of Zn, as seen in the DTA/TG data. The largely temperature-independent resistivity in $Yb_{14}MnSb_{11}$ is known to be due to the spin disorder scattering and is evident in the magnetoresistance.[12] Alloying with d^{10} Zn^{2+} lowers the spin concentration and therefore reduces the spin disorder scattering. Spin disorder scattering should be proportional to the magnitude of the spin and exchange interactions. As the hole is spin paired with the spin from the d^5 Mn ion, the effective spin is only $s = 5/2 - ½ = 2$ in $Yb_{14}MnSb_{11}$. Because the Zn is also +2, substitution of Mn for Zn maintains the hole concentration but should reduce the spin

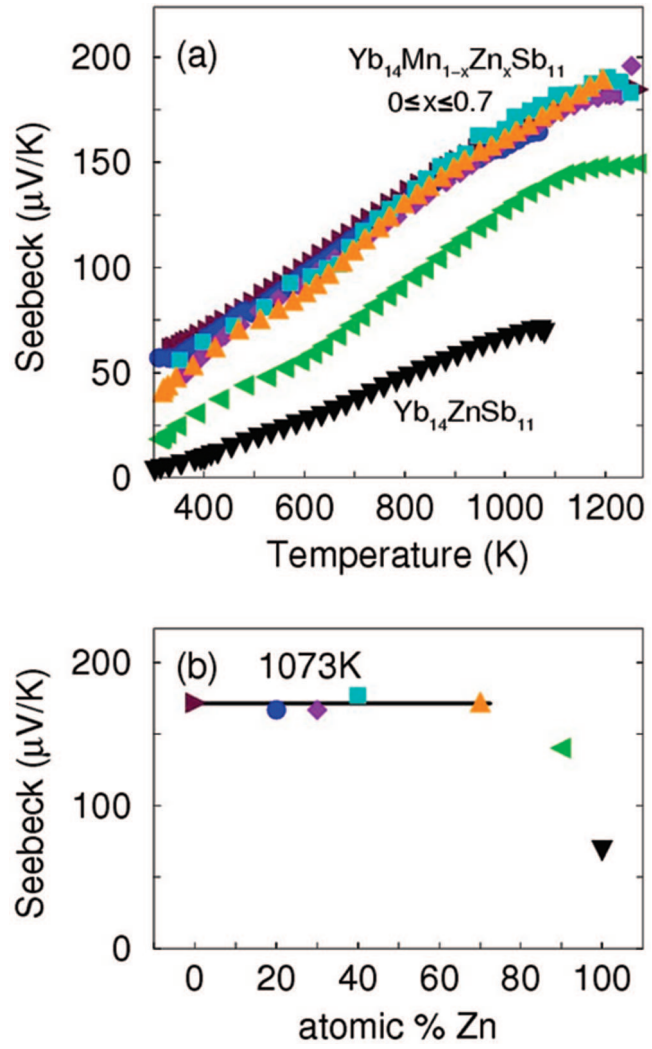

Figure 7. (a) Seebeck coefficient measurements of the $Yb_{14}Mn_{1-x}Zn_xSb_{11}$ solid solution $x = 0.0$ to 1.0. (b) The trend in the Seebeck coefficient versus composition at 1073 K. Colors and symbols for the compositions are indicated in (b).

from the d-electrons. Thus, the net spin in $Yb_{14}Mn_{1-x}Zn_xSb_{11}$ should be $s = 5/2(1-x) - ½$, which will reach zero at $x = 0.8$. This trend is shown by the dashed line in Figure 6b. For $x = 1.0$, the temperature independent term is again large because the itinerant hole now has Yb character, inducing Yb^{3+} ($\mu_{eff} = 4.5\ \mu_B$) valence fluctuations. Also included in the temperature-independent term, as expected from Matthiessen's rule, is the reduction in scattering due to point defects and grain boundaries within the material.[31] It is also possible that Zn may serve as a sintering aid to reduce grain boundary resistance.

Seebeck coefficient measurements obtained up to 1275 K reveal a larger Seebeck coefficient for $Yb_{14}MnSb_{11}$ (70 μV/K at 400 K) than for $Yb_{14}ZnSb_{11}$ (10 μV/K at 400 K) (Figure 7a). Prior studies of $Yb_{14}MnSb_{11}$ and $Yb_{14}ZnSb_{11}$ have attributed this difference in Seebeck coefficient to valence fluctuations of Yb in $Yb_{14}ZnSb_{11}$.[21] For the solid solution up to $x = 0.7$, Seebeck coefficients match that of the $Yb_{14}MnSb_{11}$ parent compound. The constant Seebeck values

(31) Kittel, C. *Introduction to Solid State Physics*, 7th ed.;John Wiley and Sons, Inc.: New York, 1996.

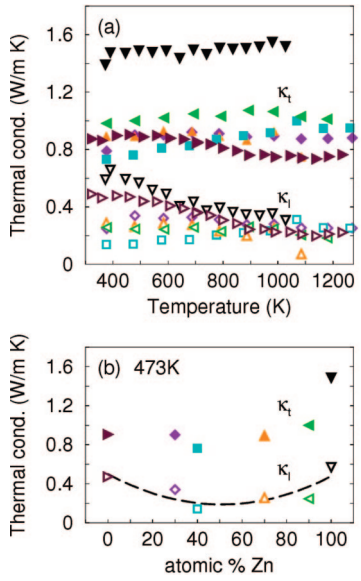

Figure 8. (a) Thermal conductivity measurements of the $Yb_{14}Mn_{1-x}Zn_xSb_{11}$ solid solution are shown in closed symbols (κ_t) and open symbols denote the lattice component of the thermal conductivity (κ_l). (b) At low temperatures, alloying decreases the lattice component of the thermal conductivity. Colors and symbols for the compositions are indicated in (b).

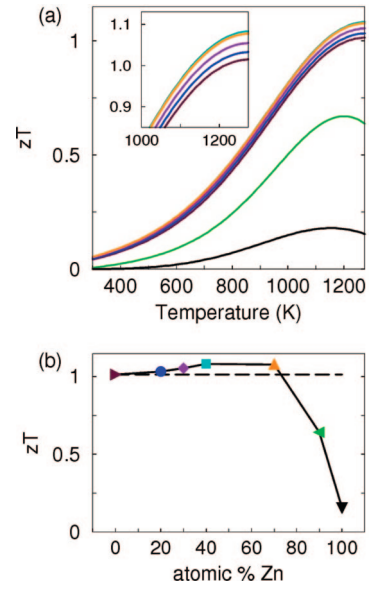

Figure 9. (a) zT values versus temperature for $Yb_{14}Mn_{1-x}Zn_xSb_{11}$. Inset shows an enlarged region of the peak zT values, with optimum performance in the $x = 0.4-0.7$ range. (b) All compositions containing significant levels of manganese exhibit zT values in excess of 1.0 at 1275 K with a maximum zT of 1.1 for the $x = 0.4$ composition. Colors and symbols for the compositions are indicated in (b).

suggest no Yb valence fluctuations for compositions $x \leq 0.7$. Above this concentration, a distinct decrease is observed as Zn begins to dominate the electronic properties. Such behavior is clearly seen in Figure 7b, which shows the Seebeck coefficient at 1073 K remaining constant across the composition range of $0 \leq x \leq 0.7$. This temperature was used to illustrate this trend as it is the maximum measured temperature of the $Yb_{14}ZnSb_{11}$. Equation 3 enables the calculation of effective mass (m^*) using the approximation of degenerate semiconductors and a charge carrier scattering distance which is independent of energy. From the carrier concentration (0.8–1.2 $\times$ 10^{21} cm^{-3}), calculated from the Hall effect measurements, and the slope of the Seebeck coefficient (0.156 $\mu V/K^2$), an average effective mass of 2.0–2.6 m_e is obtained. As we might expect for the isoelectronic substitution of Zn for Mn, Zn doping does not drastically change the carrier concentration. The band structure does not appear to change significantly with alloying, as seen in the constant effective mass. This can be expected because of the low relative concentration of transition metals in $Yb_{14}Mn_{1-x}Zn_xSb_{11}$ and the similarity in the two 3d elements. The mobility for all samples ranged from 1 to 4 $cm^2/(Vs)$.

$$\alpha = \frac{8\pi^2 k_B^2}{3eh^2} m^* T \left(\frac{\pi}{3n}\right)^{2/3} \quad (3)$$

The thermal conductivity data for the $Yb_{14}Mn_{1-x}Zn_xSb_{11}$ series as a function of temperature are shown in Figure 8a. The lattice component (κ_l) of the thermal conductivity was obtained by subtracting the electronic component (κ_e) obtained via the Wiedemann–Franz law ($\kappa_t = \kappa_e + \kappa_l$; $\kappa_e = LT\sigma$). Figure 8b represents the thermal conductivity data as a function of the Zn concentration at 473 K and shows a clear decrease in κ_l at low temperatures with increased alloy disorder. The decrease in lattice thermal conductivity is likely due to a combination of alloying and inclusions of the $Yb_9M_{4+x}Sb_9$ (M = Mn/Zn) phase. At higher temperatures, all the compositions studied converge to a constant κ_l value of ~0.25 W/(mK). Differences in high-temperature κ_l show no trend with composition and are likely a product of measurement uncertainty. Such results may be interpreted as the converging of the lattice thermal conductivity to a lower, amorphous value (minimum thermal conductivity κ_{min}) at high temperature.

For the $0 \leq x \leq 0.7$ data, we see significant changes in resistivity but insignificant changes in Seebeck coefficient and lattice thermal conductivity with changing x levels. For the purpose of calculating zT, the minor fluctuations in Seebeck coefficient were eliminated by using a single polynomial curve fit to the combined data for $0 \leq x \leq 0.7$. Likewise, the insignificant noise in thermal conductivity was eliminated by using the κ_l of $Yb_{14}MnSb_{11}$ for all Mn-containing samples, as described in the Experimental Section. As the lattice component of all Mn-containing compositions converge to the same value at high temperatures, the resulting calculated thermal conductivity curves are a reasonable fit to the data above 800 K (see the Supporting Information, Figure 1). Below 800 K, the data appears to be consistently lower than the curves, indicating that the mixed alloys have reduced lattice thermal conductivity (as discussed above).

The thermoelectric figures of merit (zT) for the Mn−Zn solid solution are shown in Figure 9a with a maximum peak value of 1.1 obtained at 1275 K for $Yb_{14}Mn_{0.6}Zn_{0.4}Sb_{11}$. A gradual improvement in zT is observed with increasing Zn concentration until $x \approx 0.4$ (Figure 9b). This increase in zT is entirely due to the decreasing electrical resistivity while maintaining a constant Seebeck curve. Beyond $x = 0.7$, the decreasing Seebeck coefficient dramatically lowers zT. A large portion of the decrease in electrical resistivity can be

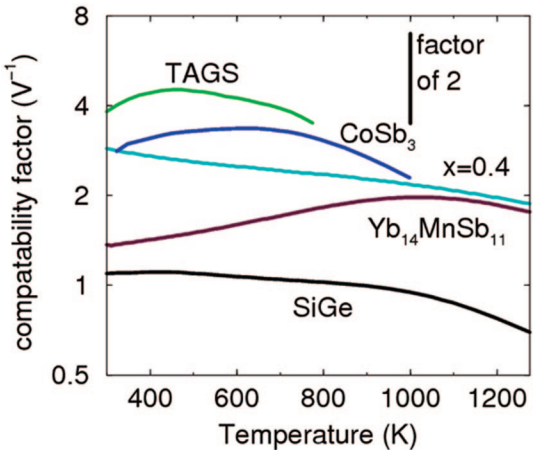

Figure 10. Calculation of the compatibility factor for $Yb_{14}MnSb_{11}$ and $Yb_{14}Mn_{1-x}Zn_xSb_{11}$ $x = 0.4$ compositions reveals that both materials are significantly more compatible than SiGe for segmenting with TAGS and skutterudite materials.

attributed to spin disorder scattering, but other effects such as grain boundary resistance may also be present.

High-efficiency segmented generators require materials with similar compatibility factors (s, eq 2). When the difference in s between two materials is greater than a factor of 2, low efficiencies will result. As can be seen in Figure 10, the optimized $x = 0.4$ composition is improved for segmentation with the lower temperature TAGS ($(GeTe)_{0.85}(AgSbTe_2)_{0.15}$) and skutterudites materials compared to the parent $Yb_{14}MnSb_{11}$ compound. Thus $Yb_{14}Mn_{0.6}Zn_{0.4}Sb_{11}$ is improved on two levels-a higher zT and an improved compatibility factor, both of which will improve a device's efficiency upon segmentation.

Conclusion

Homogeneous solid solutions of $Yb_{14}Mn_{1-x}Zn_xSb_{11}$ up through $x \leq 0.4$ have been made by a Sn-flux route and result in a continuous change of properties. Spin-disorder scattering in $Yb_{14}Mn_{1-x}Zn_xSb_{11}$ can be effectively reduced through the isoelectronic Zn substitution of the magnetic Mn ion up through $x = 0.4$. The isoelectronic substitution maintains carrier concentration and band structure thereby leaving the Seebeck coefficient unaffected. By decoupling the Seebeck coefficient and electrical resistivity, a significant gain in zT is obtained. Measurements of the optimized $x = 0.4$ composition reveal ~10% improvement over the parent $Yb_{14}MnSb_{11}$ compound.

Acknowledgment. We thank Sarah Roeske for aid with the electron microprobe, James Fettinger, and Håkon Hope for assistance with the single-crystal refinement. Catherine A. Cox was supported by a NSF funded Bridge to Doctorate fellowship. Portions of this work were carried out at the Jet Propulsion Laboratory, California Institute of Technology, under contract with NASA. This research was funded by NSF DMR-0600742 and NASA/Jet Propulsion Laboratory.

Supporting Information Available: Additional crystallographic data for $Yb_{14}Mn_{1-x}Zn_xSb_{11}$ ($x = 0.2$, 0.3, 0.4, 0.7, 0.9) in CIF format; a table of crystallographic parameters and a plot of the temperature dependence of the calculated κ_t used in the figure of merit plot (PDF). This material is available free of charge via the Internet at http://pubs.acs.org.

CM703616Q